PAPER • OPEN ACCESS

Influence of flow rate, temperature and pressure on multiphase flows of supercritical carbon dioxide and water using multivariate partial least square regression

View the article online for updates and enhancements.

Influence of flow rate, temperature and pressure on multiphase flows of supercritical carbon dioxide and water using multivariate partial least square regression

Stefan Knaust[1]**, Martin Andersson**[1]**, Niklas Rogeman**[1]**, Klas Hjort**[1]**, Gustav Amberg**[2] **and Lena Klintberg**[1]

[1] Department of Engineering Sciences, Uppsala University, Box 534, 751 21 Uppsala, Sweden
[2] Royal Institute of Technology (KTH), Stockholm Sweden

E-mail: lena.klintberg@angstrom.uu.se

Abstract

Supercritical carbon dioxide ($scCO_2$) is often used to replace harmful solvents and can dissolve a wide range of organic compounds. With a favorable critical point at 31 °C and 7.4 MPa, reaching above the critical point for $scCO_2$ is fairly accessible. Because of the compressible nature of $scCO_2$ and the large changes of viscosity and density with temperature and pressure, there is a need to determine the behavior of $scCO_2$ in microfluidic systems. Here, the influence of how parameters such as flow rate, temperature, pressure, and flow ratio affects the length of parallel flow of water and $scCO_2$ and the length of the created CO_2 segments are investigated and modeled using multivariate data analysis for a 10 mm long double-y channel. The parallel length and segment size were observed in the laminar regime around and above the critical point of CO_2. The flow ratio between the two fluids together with the flow rate influenced both the parallel length and the segment sizes, and a higher pressure resulted in shorter parallel lengths. Regarding the segment length of CO_2, longer segments were a result of a higher Weber number for H_2O together with a higher temperature in the channel.

Keywords: supercritical fluids, microfluidics, carbon dioxide, partial least square regression, principal component analysis, fluid dynamics, multiphase flow

S Online supplementary data available from stacks.iop.org/JMM/25/105001/mmedia

(Some figures may appear in colour only in the online journal)

1. Introduction

In chemistry, it is often desired to replace toxic agents with more harmless alternatives, referred to as green chemistry [1]. One agent used as a green solvent is supercritical carbon dioxide ($scCO_2$), replacing environmentally harmful solvents with similar properties [2]. A supercritical fluid has properties in-between gases and liquids, which are adjustable with pressure and temperature. The diffusivity and viscosity of a supercritical fluid is similar to that of gases while the density is in the range of liquids [3, 4]. For chemical processing, the low viscosity offer efficient extraction and separation kinetics,

while the liquid-like density will provide sufficient solute-solvent interaction. Hence, chemical processes like synthesis and extraction can be tuned by changing the pressure and temperature. $scCO_2$ can dissolve a wide range of organic compounds due to its low dipole moment, combined with Lewis acid-base interactions. Further, to configure the solubility profile, polar co-solvents such as ethanol or methanol can be added [5].

With a favorable critical point at 31 °C and 7.4 MPa, reaching above the critical point for $scCO_2$ is fairly accessible. However, because of the compressible nature of $scCO_2$ and the large changes of viscosity and density with temperature and pressure, there is a need to determine the behavior of $scCO_2$ in microfluidic systems, especially when there are multiple phases in the system, like H_2O and $scCO_2$. A typical pressure and temperature for a process is 15 MPa and 80 °C, giving a viscosity ratio of approximately 10:1 [4, 6] for H_2O and CO_2. The density ratio between the two phases is approximately 2:1 [3, 6]. To provide a stable control of multiphase systems where the two phases have radically different properties when it comes to viscosity and compressibility has been identified as one of the future challenges in microfluidics by Elvira *et al* [7]. Computational fluid dynamics (CFD) is an important tool in research as well for industrial applications, and to experimentally characterize the behavior of this type of two phase systems gives data that can be useful for validation of computational models [8, 9]. After a junction where two phases joins, depending on the system parameters, the result can either be a segmented flow, or parallel flow between the two phases. Depending on the application, one or the other is preferred [10].

As stated in [11], fluids in nature, biotechnology and chemistry are rarely single-phase. In the past, microfabrication has been demonstrated using liquid–liquid laminar flow multiphase systems [12, 13], and methods for controlling and different applications of both droplets and interfaces are summarized in [14]. As things stand, most presented multiphase $scCO_2$-microsystems utilize segmented flows, e.g. to extract vanillin from a water solution using a glass-silicon microdevice operating at 39.8 °C and 8.1 MPa to 11.1 MPa [15], and to extract different aromatic monomers from lignin oxidation products [16]. Tiggelaar *et al* studied the formation of carbamic acid from N-benzylmethylamine and CO_2, and reaction products were observed at pressures up to 30 MPa and a temperature of 100 °C inside a glass-silicon chip [17]. Marre *et al* have demonstrated a modular glass-silicon-based chip, capable of even higher temperatures and pressures, but here using segmented scH_2O multiphase systems. The fluid was heated in a confined section of the chip to 400 °C at 25 MPa while keeping the connections closer to room temperature [18]. Other applications for this chip have been quantum dot synthesis using supercritical hexane [19] and as a pressure-volume-temperature cell for $scCO_2$ where the transition from single phase to multiphase was studied [20].

There has been less studies utilizing and investigating parallel flows of $scCO_2$, although the potential use in extraction and analysis [10]. Ohashi *et al* studied extraction of tris(acetylacetonato)-cobalt(III) from $scCO_2$ into water and
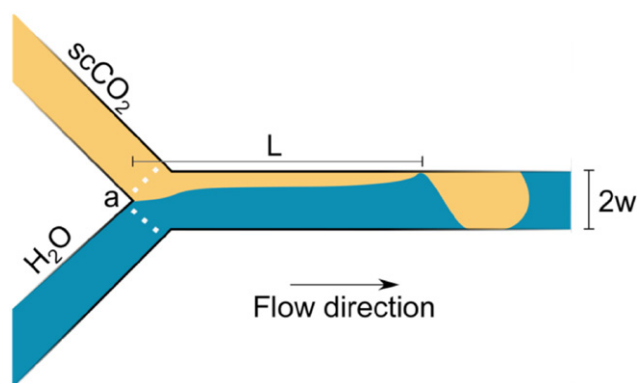

Figure 1. The inlets of the channel with the width $2w$, where Re, Ca, and We are calculated for H_2O and CO_2 at the position a, marked by dotted lines. The parallel length L is measured as the distance from where the two flows meet to where the flow breaks up into segments.

achieved a parallel flow for 0.5 s using a hydrophobic coating and having a guide in between the flows [21]. The experiment was performed at 10 MPa and 45 °C. However, only limited details of the design is mentioned by the authors.

Ogden *et al* characterized $scCO_2$-water flows for different flow rates and relative ratio of $scCO_2$ and water [22]. In all experiments, the pressure was set to 10 MPa and the temperature to 50 °C. Segmented flow was mostly observed, although parallel flow was observed for high ratios of $scCO_2$ relative to water. At high flow rates the parallel flow was observed to be instable and was denoted wavy.

Multivariate data analysis is widely used in chemistry [23] and for pharmaceutical applications [24], as well as being a valuable tool in the processing industry [25]. In microsystems, and especially in microfluidics, multivariate techniques have mainly been used to calibrate different responses to spectroscopic data generated from Raman spectroscopy [26–28] and x-ray fluorescence spectroscopy [29], or to analyze responses from microsensors or microsensor arrays [30, 31]. Here we demonstrate how multivariate data analysis can be used to model and predict segment length and parallel length in the complex multiphase system of $scCO_2$ and H_2O.

2. Theory

For microfluidic systems, dimensionless numbers are often used to characterize the properties of the flow, and for small systems where gravity is negligible, the Reynolds number (Re), capillary number (Ca) and Weber number (We) are the most interesting [32].

For our experiments, Re, Ca, and We were calculated at the entrance to the main channel, *a* in figure 1, where the flow velocity is known and only dependent on temperature and pressure.

Guillot and Colin studied water and oils with varying viscosities flowing in parallel [33]. Three different behaviors were observed; parallel, parallel broken up to segmented droplet flow, and droplets formed at the *T*-junction, the latter not having reproducible droplet sizes. For the parallel flow breaking up in the channel, they found that the stability of the

flow is linked to the confinement of the flow and cannot be described in terms of a competition between viscous forces and the capillary forces, i.e. Ca, but is determined by the channel wetting conditions, geometry and the viscosity.

Garstecki *et al* studied the mechanism of droplets breaking up in a *T*-junction for low Re of two-phase flows of silicon oil and water, and water and nitrogen gas [34]. The dominant effect of breakup was found to be the pressure-drop across the emerging segments, where the size of the segments were dependent on the viscosity of the continuous phase, the geometry of the device and the interfacial tension between the two phases.

In a review by Hessel *et al* different gas-liquid continuous phase micro reactors are presented [35]. For dispersed-phase micro reactors, the gas-liquid flow rate ratio is reported to be a key parameter to obtain annular flows, for which at high values, a thin liquid annulus film surrounds a gas core. For these micro reactors, there is generally a degree of uncertainty concerning the fluid geometries and available interfacial areas, and flow disturbances can for these systems cause entrainment of the liquid film into the gas core.

Working with fluids with varying density, the volumetric flow rate will be different inside the pump compared to the chip. By using conservation of mass, the volumetric flow rate can be modified to correct for density variations along the channel according to

$$\rho_{\text{pump}} Q_{\text{pump}} = \rho_{\text{chip}} Q_{\text{chip}}, \tag{1}$$

where Q is the volumetric flow rate and ρ is the density of the fluid. Thus, the fluid velocity on the chip, accounting for the preservation of mass, in a heated channel can be described as

$$U = \frac{Q_{\text{pump}}}{A} \frac{\rho_{\text{pump}}}{\rho_{\text{chip}}}. \tag{2}$$

where A is the fluid cross section area in the channel. Hence, the flow velocity is affected by changes in the pressure and temperature.

With multivariate data analysis it is possible to detect and model the underlying factors affecting a multivariate system. In principal component analysis (PCA), the orthogonal directions of maximum variation, i.e. the principal components (PC), are found. A score plot is generated by projecting the data, here variables and responses, on the PCs showing general trends and the plot can also be used for data classification [36]. The corresponding loading plot visualizes the relation between the variables. Partial least squares regression (PLS) is a similar procedure, but here, the covariance between the variables and the responses are maximized in order to find a linear regression model describing the system [37].

3. Experimental

3.1. Manufacturing

The chip used had a double-y channel with a 10 mm long channel, figure 2, etched from one 4″ Borofloat-33 glass wafer (Schott), the channel wafer, bonded to another Borofloat-33
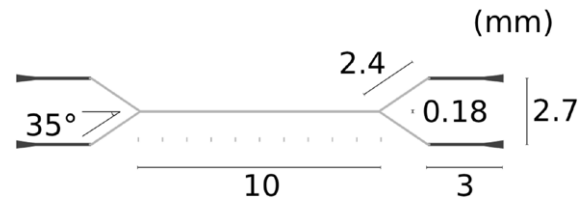

Figure 2. The chip design. The 2.4 mm long inlets meet at the 180 μm wide and 10 mm long channel at an angle of 70°. Ten markings were etched along the channel at an interval of 1 mm, used as a length reference. The chip consists of two etch depths, 40 μm (grey) and 90 μm (black), where the black areas are etched on both glass wafers. The connection trenches (black) is separated by 2.7 mm and is 3 mm long. Also, to ease the insertion of the glass capillary, the edge of the trenches are conic towards the glass edge. The inlet channels are 170 μm wide.
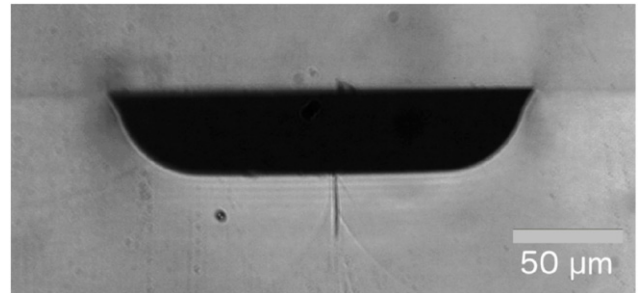

Figure 3. A cross section of the channel, which is 193 μm in width and 40 μm in height.

wafer, figure 3, only with trenches for connections etched. After etching, the channel was 40 μm in height, and 193 μm in width.

Both wafers were initially co-processed, with the second shallow etching for channels only done on the channel wafer. Processed in a cleanroom, the glass wafers were first cleaned in Piranha (1:1, H_2SO_4: H_2O_2) for 10 min, followed by RCA1 (5:1:1, DI: NH_4OH: H_2O_2) and RCA2 (5:1:1, DI: HCl: H_2O_2) at 60 °C for 10 min respectively and finally a megasonic cleaning at 60 °C for 10 min. A chromium layer (12 nm) was evaporated as an adhesion layer, followed by a gold layer of 100 nm, deposited in two steps of equal thickness with 10 min pause, without breaking the vacuum inside the evaporator. To define the pattern for connection trenches, a positive photoresist, Microposit S1813 (Dow Chemical Co.) was spun to a thickness of 1 μm and etch marks were etched in the gold layer using a gold etch (100 g KI, 25 g I2 in 100 g H_2O), after which the resist was stripped in acetone. A positive photoresist, AZ 9260 (MicroChemicals) was sprayed to a thickness of 12 μm and soft baked at 90 °C for 140 s, in which patterns for channels were developed, and the gold was stripped in the openings using the gold etch, followed by a chromium etch [$(NH_4)_2$ $Ce(NO_3)_6$ (10–15%) + HCl(15–20% + H_2O)] prepared by Sunchem AB (Sweden). Before the glass etching, the backside was protected using a surface protection film SWT 10 (Nitto). The inlets and outlets were etched isotropically for 12 min in concentrated HF, resulting in approximately 90 μm deep trenches.

The photoresist and metal masks were stripped on both wafers, and on the channel wafer, a new layer of 12 μm spray photoresist was deposited, same procedure as mentioned above,
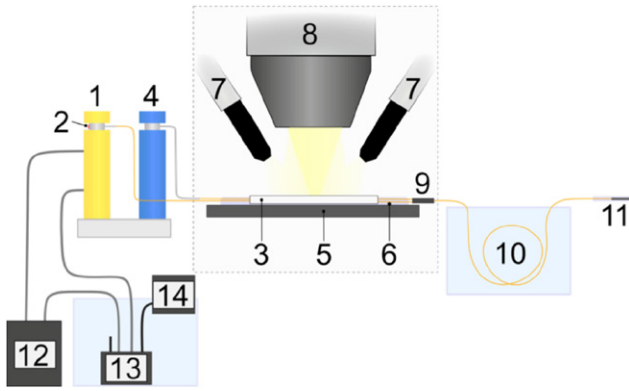
Figure 4. The experimental setup. (1) The thermally insulated CO_2 pump, with an (2) attached Pt-100 sensor, is connected to (3) the glass chip using glass capillaries for the 10 μl min^{-1} flow rates, and using stainless steel tubes for the 70 μl min^{-1} flow rates, both approximately 1 m in length. (4) The H_2O pump is connected to the capillaries of the glass chip using approximately 1 m long stainless steel tubes. The glass chip is attached to (5) a heating stage using (6) thermal grease covering both inlet an outlet capillaries. For imaging, the glass chip is lit up by (7) two directional lamps and is viewed by (8) a microscope connected to a high-speed camera. The outlet capillaries are connected at (9) a *T*-junction to the (10) flow-restricting capillary submerged in a temperature controlled water bath. To prevent ice-clogging from the expanding gas, the capillary end is placed inside (11) a heater. To cool the CO_2 pump (12) a compressor is connected to (13) a parallel plate heat exchanger submerged in a water bath. Also connected to the heat exchanger is (14) a heater, used to circulate the water and to control the temperature.

in which the channels were patterned. After removing the chromium and gold in the openings, the wafer was etched in concentrated HF for 4.5 min, resulting in a depth of 40 μm, again protecting the backside with the surface protection film. The etch depth was controlled using a Dektak 150 (Veeco) profilometer. After etching, the photoresist and metal masks were stripped.

Prior to bonding, the wafers were cleaned according to the procedure mentioned above, i.e. Piranha, RCA1, RCA2, and megasonic cleaning. To minimize the risk of particles affecting the bond quality, the bonding was done within 10 min after the cleaning. The wafers were manually aligned under a microscope and before the annealing the wafers were pressurized by 1 kg for 60 min. The fusion bonding was done in a vertical furnace at 625 °C for 6 h, with the glass wafers supported by a silicon nitride wafer to prevent bulging.

After bonding, the wafers were diced using a saw DAD 361 (Disco). To support the glass wafers during dicing, the wafers were glued onto a silicon wafer using thermoplastic glue Crystalbond 509 (SPI Supplies), soluble in acetone. After dicing, the chips were removed and carefully cleaned several times in ultrasonic acetone baths to remove any residues from the dicing and glue. Glass capillaries (i.d. 75 μm, o.d. 150 μm) were glued to the outlets using a fast curing epoxy Araldite Rapid (huntman advanced materials).

3.2. Setup

Two high-pressure syringe pumps, DM100 (Teledyne Isco), were used to supply the two flows of deionized H_2O and food graded CO_2 (SodaStream) to the glass chip, figure 4. The

CO_2 tower was cooled down to 13.5 °C using a compressor, FC200 (Julabo). As the compressor had a known temperature variation of approximately 1 °C over a 30 min period, the compressor was connected in series with a counter current heat exchanger, submerged in a 10 l H_2O bath. Using an E100 heater (Lauda), the bath was heated to 14 °C. This resulted in temperature variations of approximately 0.1 °C, which caused the flow rate to vary by approximately by 1 μl min^{-1} at 10 MPa because of the change in density. For the lower flow rates of 10 μl min^{-1}, the thermally induced flow variations of 1 μl min^{-1} were considered too large. Hence, the compressor was changed to a more powerful RK20 (Lauda), for which the cyclic behavior of the temperature variation was no longer visible and the CO_2 tower was cooled down to 8 °C.

To regulate the chip pressure, a 12.5 m long capillary, i.d. 75 μm, was used for the flow rates of 70 μl min^{-1}, and 1.5 m long capillary, i.d. 25 μm for 10 μl min^{-1}.

The chip was attached to a heating stage with resistively heated Kanthal wires using thermal grease, and the temperature was set using a constant power from a power supply QL335TP (TTi).

The temperature was logged at 0.3 Hz at the heating stage and at the top of the CO_2 pump using Pt-100 sensors using a four-wire configuration, and in the H_2O bath at the pressure regulating capillary using a thermocouple type K.

The capillary of the glass chip was connected to the syringe pump tubing using PEEK sleeves and fittings. To prevent air convection from affecting the CO_2 flow, the stainless steel tube supplying the CO_2 from the pump was thermally insulated by being feed through a PVC tube. To minimize the dead volume for the lower flow rates, the 1 m long stainless steel tube was replaced with a 1 m, i.d. 75 μm capillary, which was not possible to use at higher flow rates because the large flow restriction.

The outlet capillary was submerged in a temperature regulated H_2O bath to provide thermal stability and to be able to change the pressure by varying the bath temperature, i.e. changing the viscosity of the fluid passing through. As an approximation, the pressure drop is determined by the Hagen–Poiseuille equation,

$$\Delta P = \frac{8\eta L Q}{\pi r^4}, \tag{3}$$

valid for an incompressible fluid. However, using H_2O and CO_2 at high pressures will result in a compressible two-phase flow, which requires a more complex model for describing the pressure drop. Based on the pressure drop from a completely H_2O filled capillary, which decreases approximately 30% for a 1:1 CO_2:H_2O-flow, this approximation was found to be good enough as a rough estimation to determine the outlet capillary length. To prevent ice clogging at the outlet caused by the expanding gas, the capillary end was placed inside a wired heater and set to approximately 90 °C.

The glass chip was imaged using a high-speed camera, Phantom Miro M310 (Vision Research) at 2500 fps.

3.3. Procedure

To build up pressure during the initial compression phase of CO_2, a higher volumetric flow rate was used with a higher

Table 1. Variables used in PCA model.

Variable	Unit	Dependencies	Description
P	MPa		Measured system pressure at the H_2O pump.
T	°C		Measured temperature of the glass chip.
$T_{CO_2,pump}$	°C		Measured temperature of the CO_2 pump.
Q_{CO_2}	$\mu l\,min^{-1}$		Measured flow rate of CO_2 at the pump.
Q_{H_2O}	$\mu l\,min^{-1}$		Measured flow rate of H_2O at the pump.
L/w			Measured parallel length divided by channel width.
s/w			Measured segment size of CO_2 divided by channel width.
$\rho_{CO_2,pump}$	$kg\,m^{-3}$	$P, T_{CO_2,\,pump}$	Interpolated density from tabulated data [3] of CO_2 inside the pump.
$\rho_{CO_2,chip}$	$kg\,m^{-3}$	P, T	Interpolated density from tabulated data [3] of CO_2 at the chip.
$\eta_{CO_2,chip}$	Pa s	P, T	Interpolated viscosity from tabulated data [4] of CO_2 at the chip.
$\rho_{H_2O,pump}$	$kg\,m^{-3}$	P	Interpolated density from tabulated data [6] of H_2O inside the pump.
$\rho_{H_2O,chip}$	$kg\,m^{-3}$	P, T	Interpolated density from tabulated data [6] of H_2O inside the chip.
$\eta_{H_2O,chip}$	Pa s	P, T	Interpolated viscosity from tabulated data [6] of H_2O at the chip
γ	$N\,m^{-1}$	P, T	Interpolated interfacial tension from tabulated data [32, 33] between CO_2 and H_2O at the chip.
Q_{total}	$\mu l\,min^{-1}$	Q_{CO_2}, Q_{H_2O}	Calculated total flow rate of the two pumps at the pumps.
$Q_{ratio,pump}$		Q_{CO_2}, Q_{H_2O}	Calculated ratio of CO_2:H_2O at the pumps.
$Q_{CO_2,chip}$	$\mu l\,min^{-1}$	$Q_{CO_2}, \rho_{CO_2,pump}, \rho_{CO_2,chip}$	Calculated flow rate of CO_2 at the chip.
$Q_{H_2O,chip}$	$\mu l\,min^{-1}$	$Q_{H_2O}, \rho_{H_2O,pump}, \rho_{H_2O,chip}$	Calculated flow rate of H_2O at the chip.
$Q_{total,chip}$	$\mu l\,min^{-1}$	$Q_{CO_2,chip}, Q_{H_2O,chip}$	Calculated total flow rate of the two pumps at the chip.
$Q_{ratio,chip}$		$Q_{CO_2,chip}, Q_{H_2O,chip}$	Calculated ratio of CO_2:H_2O at the chip.
Re_{CO_2}		$Q_{CO_2,chip}, \rho_{CO_2,chip}, \eta_{CO_2,chip}$	Calculated Re for the CO_2 flow.
Ca_{CO_2}		$Q_{CO_2,chip}, \eta_{CO_2,chip}, \gamma$	Calculated Ca for the CO_2 flow.
We_{CO_2}		$Q_{CO_2,chip}, \rho_{CO_2,chip}, \gamma$	Calculated We for the CO_2 flow.
Re_{H_2O}		$Q_{H_2O,chip}, \rho_{H_2O,chip}, \eta_{H_2O,chip}$	Calculated Re for the H_2O flow.
Ca_{H_2O}		$Q_{H_2O,chip}, \eta_{H_2O,chip}, \gamma$	Calculated Ca for the H_2O flow.
We_{H_2O}		$Q_{H_2O,chip}, \rho_{H_2O,chip}, \gamma$	Calculated We for the H_2O flow.

ratio of CO_2 to H_2O (approximately 2.5:1), until a stable pressure was reached to keep a similar ratio between CO_2 and H_2O at the outlet capillary, as a H_2O filled capillary would result in a higher flow resistance, and hence give an initially higher back pressure.

For the 50 measurements performed, two flow rates were investigated, 70 $\mu l\,min^{-1}$ and 10 $\mu l\,min^{-1}$, with the relative ratios between the CO_2 pump and the H_2O pump of 4:9, 1:1, and 9:4, measured and controlled at the pumps.

Low ratio of CO_2 (4:9) resulted in a rapid breakage of the devices, hence only a limited number of measurements were carried out for this ratio.

For all experiments, the chip pressure is assumed to be equal to the pressure inside the H_2O pump, because the large inner diameter of the stainless steel tube of 1 mm between the chip and the pump. Being approximately 60 cm long, this will only result in a pressure drop in the order of 0.2 kPa for a pure H_2O flow of 35 $\mu l\,min^{-1}$. The system pressure varied between 9.5 MPa and 17 MPa by varying the length and temperature of the outlet capillary, and for each set of flow rate and

pressure, the sample temperature was swept, starting at 50 °C, decreasing in steps of 10 °C down to 25 °C (below the critical temperature). At these conditions, the density for CO_2 varied between 350 kg m^{-3} and 860 kg m^{-3}, and the dynamic viscosity for CO_2 varied between 30 μPa s and 83 μPa s. Before each measurement, the logged temperatures and pressures were allowed to stabilize until no trend of increase or decrease in pressure and temperature was seen for at least 10 min.

3.4. PLS-modeling

The multivariate analysis was done using Simca-P 13.0 (Umetrics). The general trends in the data set were investigated with PCA. For each set of pressure and temperature at the chip, interpolated values of tabulated data for density [3, 6], viscosity [4, 6], and interfacial tension between CO_2 and H_2O [38, 39], respectively, and calculated values of Re, We and Ca for both the CO_2 flow and H_2O flow, were all initially used along with the flow rate of the two pumps, summarized in table 1. The length of the parallel flow, *L*, divided by half the

Table 2. The range of the dimensionless numbers for CO_2 and H_2O, calculated at the inlet of the channel for the two flow rates.

Flow rate (μl min^{-1})	Re	Ca ($\times 10^{-5}$)	We ($\times 10^{-5}$)
CO_2			
10	8.5–19	2.9–4.2	29–71
70	31–147	13–40	640–3800
H_2O			
10	0.6–1.0	15–27	11–23
70	3.1–8.8	110–400	530–2150

Figure 6. PCA score plot with the observations divided into three categories; *e* for segments created at the entrance, *s* for segments created along the channel, and *p* for parallel flow throughout the channel. Next to each measurement is the observed parallel length (L/w). The score values (*t*) along the first PC are plotted along the *x*-axis *t* [1], and the score values along the second PC are plotted against the *y*-axis *t* [2]. The influence of flow rate is separating the data into two groups along PC1, while the observations arranges according to the categories mentioned along PC2, with a longer parallel length in the negative direction.

Figure 5. Three different regimes were observed between CO_2 (yellow) and H_2O (blue). (a) Parallel flow for 45 μl min^{-1} CO_2, 25 μl min^{-1} H_2O at 12 MPa and 50 °C. (b) Parallel flow broken up in segments for 35 μl min^{-1} CO_2, 35 μl min^{-1} H_2O for 14 MPa and 42 °C. (c) Segments formed at the inlets for 5 μl min^{-1} CO_2, 5 μl min^{-1} H_2O at 11 MPa and 51 °C. The colors were added during post processing together with some coordinates in mm measured from the junction.

channel width i.e. the initial flow width, w, figure 1, together with the length of CO_2 segments, *s*, also divided *w*, were used as responses for making two different PLS models. All variables were normalized and centered, and as part of the modeling process, the variables that influence the responses were found. Some of the investigated variables have covariance, and in the final models, the variables that have the best correlation with the responses were chosen. In total there were 50 observations in the data set. Out of these, 45 observations where randomly chosen for the PLS modeling and the remaining 5 was used for model validation.

4. Results

The dimensionless numbers are presented in table 2 for the CO_2 flow and the H_2O flow, calculated at the inlets to the main channel in accordance with figure 1, Re is within the non-turbulent regime, i.e. Re $\ll$ 2000 for both the H_2O flow and the CO_2 flow at the inlet. For all the dimensionless numbers, the values for the CO_2 flow is typically one order of magnitude higher compared to the values for the H_2O flow. Three different behaviors were observed; parallel flow through the channel, figure 5(a), parallel flow broken up in segments, figure 5(b), and segmented flow from chip entrance, figure 5(c). For parallel flows extending beyond 1 mm, the
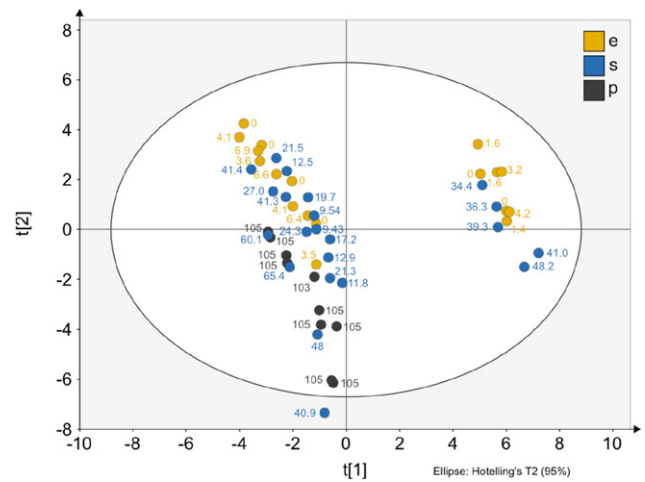
CO_2-flow was observed to be pushed to the side of the channel at a width estimated at a top down view to be within 30 to 50 μm as seen in figure 5(a).

With PCA, four PCs explain 0.96 of the variation. Together, the two first PCs explain 0.73 and are the most important. The observations in the score plot, figure 6, forms two separate groups depending on flow rate. The flow rate for the large left group was 70 μl min^{-1} and the smaller right group had a flow rate of 10 μl min^{-1}. The normalized parallel length, L/w, for each observation is shown next to each observation in figure 6, and within the two groups, the observations having longer parallel length have a tendency to have a lower score value *t* [2] along PC2, i.e. the *y*-axis. This becomes clearer when the observations is classified into three different categories; *e* (green) for segments created at the inlet with a parallel length below 0.6 mm, *s* (blue) for segments created along the channel and *p* (red) for observations with parallel lengths beyond 9.5 mm. The corresponding loading plot is showed in figure 7, and table 1 lists all the variables in the loading plot. Along PC2, observations with high parallel length L/w is positively correlated to the variables with negative loading values *p* [2] in figure 6, e.g. Q_{ratio}, and Re_{CO_2}, while variables like pressure (*P*) is negatively correlated along same axis. From figure 7, it can also be concluded that a few of the observations where the flow is parallel through the channel overlaps with some points where the segments form half way in the channel. This indicates that the fully parallel regime *p* is also affected by unknown variables not included in the model. The difference in segment length of CO_2, *s/w*, is instead manifested primarily along PC1, and e.g. a high segment length is positively correlated to a high temperature T and negatively correlated to a high total flow Q_{total}.
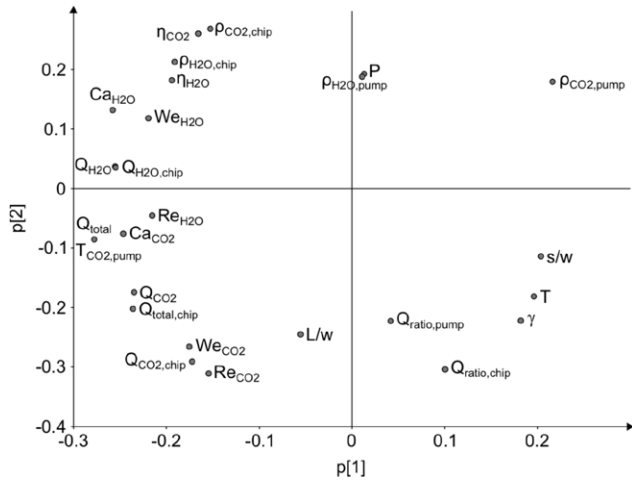
Figure 7. PCA loading plot with the variables used in the PCA model including the responses *L/w* and *s/w*. The loading values (*p*) along the first PC are plotted along the *x*-axis *p* [1], and the loading values along the second PC are plotted against the *y*-axis *p* [2].

Many of the variables co-depend on each other, and during the PLS modelling all variables that did not contribute to a higher quality factor Q^2 could be removed without affecting the amount of explained variation.

For the parallel length using 45 of the observations, the best model to predict the normalized parallel length was using P, total flow rate at the pumps (Q_{total}), and the ratio between CO_2 and H_2O at the pumps ($Q_{ratio,pump}$), for 1 PC according to

$$\frac{L}{w} = 75.8 - 9.9P + 0.29Q_{total} + 46.9Q_{ratio,pump}. \qquad (4)$$

The model using these three variables resulted in an explained variation of predicted length (R^2Y) of 0.69, and a predictive ability calculated by cross-validation (Q^2) of 0.68. Using the five observations in the prediction dataset resulted in a root mean square error of prediction (RMSEP) of 14.6, figure 8, i.e. a standard deviation of 1.4 mm in the prediction of the normalized parallel length (stacks.iop.org/JMM/25/105001/mmedia).

Modeling the normalized CO_2 segment length (*s/w*) using 34 data points out of the 45 observations where a segment length could be extracted, increasing temperature, decreasing adjusted total flow rate, increasing CO_2-ratio and an increasing We_{H_2O} increased the CO_2 segment length for 3 PCs according to

$$\frac{s}{w} = -3.84 + 0.11T - 0.11Q_{total,chip} + 5.99Q_{ratio,chip}$$
$$+ 414We_{H_2O}. \qquad (5)$$

The model using these four variables resulted in an explained variation of predicted segment length (R^2Y) of 0.84, and a predictive ability calculated by cross-validation Q^2 of 0.73. Using the 3 prediction observations where the flow actually was segmented resulted in a RMSEP of 0.48, figure 9, i.e. a standard deviation of 46 μm in the prediction of the normalized segment length.
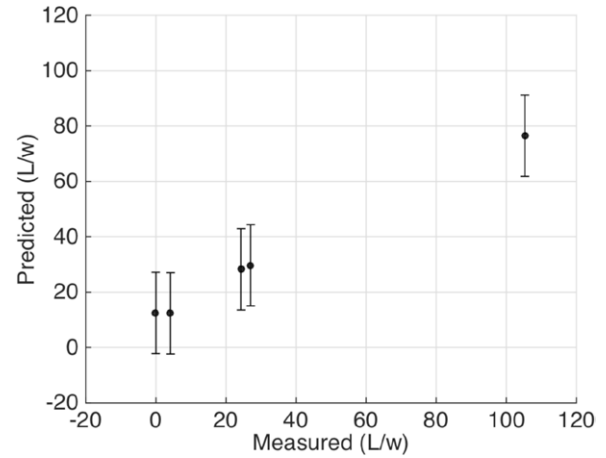

Figure 8. The measured parallel length compared to the predicted parallel length by the model for the parallel length. The error bars represent the RMSEP of the model of 14.6, i.e. and standard deviation of 1.4 mm.
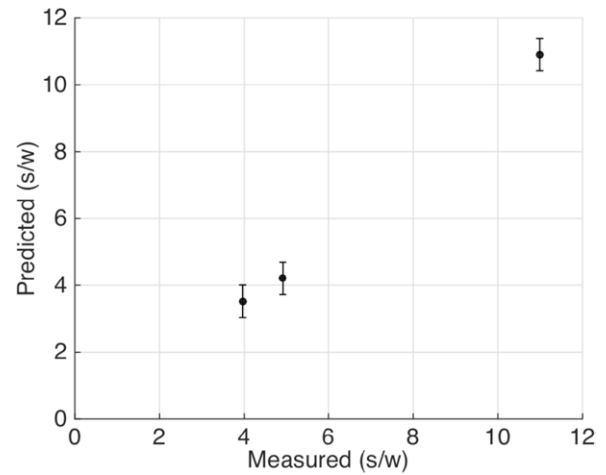

Figure 9. The measured scCO$_2$ segment length compared to the predicted length by the model. The error bars represent the RMSEP of the model of 0.48, i.e. and standard deviation of 46 μm.

5. Discussion

The glass surface favors wetting of H_2O over CO_2, causing instability in the system that eventually leads to H_2O wrapping around CO_2, and finally pinching off the flow into segments. But the observed parallel lengths were considerably longer compared to what would be the case if this wetting instability limited the parallel length. If this mechanism causes the segmentation, a rough estimation of the length scale before segmentation can be done since Ca roughly describes the velocity of this movement for Ca in the range 0.1 to 1 according to

$$U \sim 0.1\frac{\gamma}{\eta}. \qquad (6)$$

Hence, for the flow width of 95 μm, the pinching movement is expected to occur in the order of 15 μs to 30 μs for the conditions in this study, for which the flows only travels up to

5 μm down the channel. This indicates that other factors affect the break up into segments.

The dimensionless numbers used were calculated at the inlets to the channel. Since the CO_2 is pushed to the side, this leads to higher flow velocities for CO_2 and the opposite for H_2O. The actual Re in the channel will therefore be higher for CO_2 and lower for H_2O. Attempts to estimate the flow conditions inside the two-phase channel was hampered by only having access to the top down view of the cross sectional area.

In the PCA model, the observations arranged themselves in two groups with respect to the flow rate along the first PC, and further sorted, mostly along the second PC, according to the parallel length. However, for the longest parallel lengths, observation for both fully parallel measurements and segmented flows are overlapping, which indicates an unstable region.

As mentioned in another study [22], high ratios of CO_2 at high flow rates are favorable for a parallel flow. Modeling the parallel length using PLS, a longer predicted parallel length was acquired for increasing CO_2:H_2O ratio, as well as increasing the total flow rate along with a decreasing pressure. Interestingly, an increased predictability of the model was acquired when using the flow rates that were not adjusted for the variations of density. A higher flow rate is also reasonable to associate with a higher parallel length as the inertia is increased for the two fluids, preventing the pinching of the CO_2 flow.

For the 10 measurements in the category *p*, the parallel lengths exceeds the length of the channel for 9 of the measurements which is a drawback when making a model that is able to correctly predict also the longest parallel flows. However, these measurements are important information to have for predicting parallel lengths beyond 40 channel widths, i.e. approximately a third of the channel length. If these measurements are excluded, a model for the shorter parallel lengths can be created, having an explained variation of 0.72 ($Q^2 = 0.7$) and for this model, the total flow rate is not longer a significant variable.

In contrast to the model for the parallel length, the segment size is dependent on the temperature at the chip and We_{H_2O}, as well as the CO_2:H_2O ratio at the chip together with the flow rate at the chip, where the flow rate is adjusted for the density change from pump to the chip. A higher flow rate will result in longer CO_2 segments, as will increasing the ratio of CO_2, which is expected. Also, increasing the We_{H_2O} increases the segment length, which could be explained by a higher inertia that prevents the pinching movement from breaking up the CO_2 flow. The segment length was also possible to predict using We_{CO_2} instead of We_{H_2O}, although the use of We_{CO_2}, resulted in a decrease of approximately 0.04 in explained variance.

Our study does not include the heat transfer of the fluids. Hence, momentarily local variations of temperature during the compression and expansion of the CO_2 is not considered.

For our measurement setup, the global temperature is very stable, and the flow from the pumps has very little variation. However, using a passive backpressure regulator that relies on the flow resistance of the fluid passing through, the system becomes less stable as the flow resistance is different for the two fluids. As the actual volumetric ratio of CO_2 compared to H_2O increases, the flow resistance will decrease reducing the pressure and increasing the volumetric flow rate ratio even further. Hence, it is important to compensate for the different compression of the fluids during the pressure buildup in order to find the pressure giving a constant flow resistance. Working with fluids with different compressibility at high pressures gives this very different behavior, not present working with incompressible fluids. Therefore, the measurements were acquired only after no trend of increase or decrease in pressure was observed for at least 10 min.

The variation of viscosity and density for CO_2 becomes smaller at higher temperatures and pressures. As the density increases, so does the solvent power of CO_2. For controlled extraction experiments at macro scale, typical pressures and temperatures involving scCO$_2$ is above 15 MPa, and 80 °C, respectively, where the variation in densities are not as large as for the lower regions closer to the critical point. Hence, it would be beneficial to increase the temperatures and pressures. However, the glass chip durability has an upper limit, and in accordance with Tiggelaar [17], attempts to increase the temperature above 55 °C at high pressures have resulted in failures, where the crack almost always occurred at the inlets/outlets. In this study, increasing the pressure above 16 MPa, the devices only survived for a short period of time, seldom enough to stabilize the system, while staying below that pressure the devices could be pressurized for several days.

6. Conclusions

Principal component analysis (PCA) and partial least square regression (PLS) were shown useful to predict and model the behavior of multiphase flows of supercritical carbon dioxide and water.

In the PCA, lower score values along PC2 corresponded to longer parallel length and data that had been classified as parallel, segmented and segmented from the entrance formed groups in the plot.

Using PLS to model the parallel length showed that higher flow rates of CO_2 had a positive influence on the parallel length, while a higher pressure resulted in a shorter parallel length.

The length of created CO_2 segments were dependent on the temperature together with the flow rate ratio, and volumetric flow rate, both adjusted for the lower density inside the channel. Also, a higher Weber number for the H_2O flow resulted in longer CO_2 segments.

Acknowledgment

References

[1] Sanderson K 2011 It's not easy being green *Nature* **469** 18–20
[2] Raveendran P, Ikushima Y and Wallen S L 2005 Polar attributes of supercritical carbon dioxide *Acc. Chem. Res.* **38** 478–85
[3] Span R and Wagner W 1996 A new equation of state for carbon dioxide covering the fluid region from the triple-point temperature to 1100 K at pressures up to 800 MPa *J. Phys. Chem. Ref. Data.* **25** 1509–96
[4] Vesovic V, Wakeham W, Olchowy G, Sengers J, Watson J and Millat J 1990 The transport properties of carbon dioxide *J. Phys. Chem. Ref. Data.* **19** 763–808
[5] Lang Q and Wai C M 2001 Supercritical fluid extraction in herbal and natural product studies—a practical review *Talanta* **53** 771–82
[6] Lemmon E W 2011 Thermophysical properties of water and steam *CRC Handbook of Chemistry and Physics vol 92* ed W M Haynes (Boca Raton, FL: CRC Press) pp 6–10
[7] Elvira K S, i Solvas X C, Wootton R C and deMello A J 2013 The past, present and potential for microfluidic reactor technology in chemical synthesis *Nat. Chem.* **5** 905–915
[8] Martin S and Williams J R 2009 *Multiphase Flow Research* (New York: Nova Science Publishers Inc) ISBN 9781606924488
[9] Wörner M 2012 Numerical modeling of multiphase flows in microfluidics and micro process engineering: a review of methods and applications *Microfluid. Nanofluidics* **12** 841–86
[10] Aota A, Mawatari K and Kitamori T 2009 Parallel multiphase microflows: fundamental physics, stabilization methods and applications *Lab Chip* **9** 2470–6
[11] Shui L, Eijkel J C T and van den Berg A 2007 Multiphase flow in micro- and nanochannels *Sensors Actuators* B **121** 263–76
[12] Kenis P J, Rustem A, Ismagilov F and Whitesides G M 1999 Microfabrication inside capillaries using multiphase laminar flow patterning *Science* **285** 83–5
[13] Gargiuli J, Shapiro E, Gulhane H, Nair G, Drikakis D and Vadgama P 2006 Microfluidic systems for in situ formation of nylon 6,6 membranes *J. Membr. Sci.* **282** 257–65
[14] Shui L, Eijkel J C T and van den Berg A 2007 *Adv. Colloid. Interface Sci.* **133** 35–49
[15] Assmann N, Kaiser S and von Rohr P R 2012 Supercritical extraction of vanillin in a microfluidic device *J. Supercrit. Fluids* **67** 149–54
[16] Assmann N, Werhan H, Ładosz A and von Rohr P R 2013 Supercritical extraction of lignin oxidation products in a microfluidic device *Chem. Eng. Sci.* **99** 177–183
[17] Tiggelaar R M, Benito-López F, Hermes D C, Rathgen H, Egberink R J, Mugele F G, Reinhoudt D N, van den Berg A, Verboom W and Gardeniers H J 2007 Fabrication, mechanical testing and application of high-pressure glass microreactor chips *Chem. Eng. J.* **131** 163–70
[18] Marre S, Adamo A, Basak S, Aymonier C and Jensen K F 2010 Design and packaging of microreactors for high pressure and high temperature applications *Ind. Eng. Chem. Res.* **49** 11310–20
[19] Marre S, Park J, Rempel J, Guan J, Bawendi M G and Jensen K F 2008 Supercritical continuous-microflow synthesis of narrow size distribution quantum dots *Adv. Mater.* **20** 4830–4
[20] Pinho B, Girardon S, Bazer-Bachi F, Bergeot G, Marre S and Aymonier C 2014 A microfluidic approach for investigating multicomponent system thermodynamics at high pressures and temperatures *Lab Chip* **14** 3843–9

[21] Ohashi A, Sugaya M and Kim H B 2011 Development of a microfluidic device for measurement of distribution behavior between supercritical carbon dioxide and water *Anal. Sci.* **27** 567–9
[22] Ogden S, Bodén R, Do-Quang M, Wu Z, Amberg G and Hjort K 2014 Fluid behavior of supercritical carbon dioxide with water in a double-y-channel microfluidic chip *Microfluid. Nanofluidics* **17** 1105–12
[23] Lavine B and Workman J 2010 Chemometrics *Anal. Chem.* **82** 4699–711
[24] Gabrielsson J, Lindberg N-O and Lundstedt T 2002 Multivariate methods in pharmaceutical applications *J. Chemom.* **16** 141–60
[25] Xie L, Littler T and Kruger U 2012 *Statistics in Practice: Advances in Statistical Monitoring of Complex Multivariate Processes with Applications in Industrial Process Control* (West Sussex: Wiley)
[26] Komatsubara M, Namazu T, Naka N, Kashiwagi S, Ohtsuki K and Inoue S 2009 Non-destructive quantitative measurement method for normal and shear stresses on single-crystalline silicon structures for reliability of silicon *Proc. IEEE Micro Electro Mechanical Systems (MEMS)* (*Sorrento, Italy, 25–29 January 2009*) pp 657–60
[27] Xu C, Barnes S E, Wu T, Fischer D A, DeLongchamp D M, Batteas J D and Beers K L 2006 Solution and surface composition gradients via microfluidic confinement *Adv. Mater.* **18** 1427–30
[28] Barnes S E, Cygan Z T, Yates J K, Beers K L and Amis E J 2006 Raman spectroscopic monitoring of droplet polymerization in a microfluidic device *Analyst* **131** 1027–33
[29] Zhang W, Zhang Y, Chen D, Zhang R, Yu X, Gao Y, Wang C, Liu J, Zhao N and Liu W 2013 Quantitative analysis of overlapping x-ray fluorescence spectra for Ni, Cu, Zn in Soil by orthogonal signal correction and partial least squares algorithm *Adv. Mater. Res.* **705** 70–4
[30] Udina S, Carmona M, Pardo A, Calaza C, Santander J, Fonseca L and Marco S 2012 A micromachined thermoelectric sensor for natural gas analysis: multivariate calibration results *Sensors Actuators* B **166–167** 338–48
[31] Scott S, James D and Ali Z 2006 Data analysis for electronic nose systems *Microchim. Acta* **156** 183–207
[32] Squires T M and Quake S R 2005 Microfluidics: fluid physics at the nanoliter scale *Rev. Mod. Phys.* **77** 977–1026
[33] Guillot P and Colin A 2005 Stability of parallel flows in a microchannel after a T junction *Phys. Rev.* E **72** 066301
[34] Garstecki P, Fuerstman M J, Stone H A and Whitesides G M 2006 Formation of droplets and bubbles in a microfluidic T-junction—scaling and mechanism of break-up *Lab Chip* **6** 437–46
[35] Hessel V, Angeli P, Gavriilidis A and Löwe H 2005 Gas–liquid and gas–liquid–solid microstructured reactors: contacting principles and applications *Ind. Eng. Chem. Res* **44** 9750–69
[36] Wold S, Esbensen K and Geladi P 1987 Principal component analysis *Chemometr. Intell. Lab.* **2** 37–52
[37] Wold S, Sjöström M and Eriksson L 2001 PLS-regression: a basic tool of chemometrics *Chemometr. Intell. Lab.* **58** 109–30
[38] Hebach A, Oberhof A, Dahmen N, Kögel A, Ederer H and Dinjus E 2002 Interfacial tension at elevated pressures—measurements and correlations in the water + carbon dioxide system *J. Chem. Eng. Data* **47** 1540–6
[39] Chiquet P, Daridon J-L, Broseta D and Thibeau S 2007 CO_2/water interfacial tensions under pressure and temperature conditions of CO_2 geological storage *Energy Convers. Manage.* **48** 736–44